Composites: Part A 59 (2014) 57–69

Contents lists available at ScienceDirect

Composites: Part A

journal homepage: www.elsevier.com/locate/compositesa

Fracture behavior of epoxy nanocomposites modified with polyol diluent and amino-functionalized multi-walled carbon nanotubes: A loading rate study

K.C. Jajam [a], M.M. Rahman [b], M.V. Hosur [c], H.V. Tippur [a,*]

[a] Department of Mechanical Engineering, Auburn University, Auburn, AL 36849, USA
[b] Department of Mechanical Engineering, Tuskegee University, Tuskegee, AL 36088, USA
[c] Department of Materials Science and Engineering, Tuskegee University, Tuskegee, AL 36088, USA

ARTICLE INFO

Article history:
Received 22 April 2013
Received in revised form 21 October 2013
Accepted 30 December 2013
Available online 8 January 2014

Keywords:
A. Polymer–matrix composites (PMCs)
B. Fracture
D. Optical microscopy Physical methods of analysis
E. Thermosetting resin

ABSTRACT

The synergistic effects of reactive polyol diluent and amino-functionalized multi-walled carbon nanotubes on fracture of two- and three-phase (hybrid) epoxy nanocomposites are investigated under quasi-static and dynamic loading conditions. Digital image correlation method with a drop-tower and high-speed camera are used for dynamic tests. The crack-tip deformation histories and fracture parameters for stationary and growing cracks are extracted. Tests show improved crack initiation toughness in modified-epoxies relative to the neat resin with the highest enhancement in hybrid nanocomposites. The dynamic crack initiation toughness values are found to be consistently lower than the static counterparts. Fractographic examinations reveal distinct rate-dependent morphologies.

1. Introduction

Polymer matrix composites (PMCs) have been widely used in a variety of engineering applications. Among the various matrix systems, epoxy resins are commonly used due to their physical, thermo-mechanical and dielectric attributes. However, their brittleness often leads to structural damages due to poor crack growth resistance. A common approach to improve damage tolerance is to incorporate rubber particles [1–3], thermoplastics [4–6] or stiff fillers [7–9] that alter the overall mechanical and fracture performances favorably [10,11]. The rubbery or thermoplastic phases, however, generally improve ductility but diminish stiffness of thermoset resins whereas the rigid inorganic inclusions such as silica and alumina improve stiffness and strength at the expense of ductility. In addition to the type of fillers, other studies [12–17] on particulate PMCs suggest that fracture toughness can be affected by various factors such as filler size, shape, volume fraction, filler–matrix adhesion strength and the loading rate.

An alternative approach to counteract the reduction in thermo-mechanical properties of PMCs is simultaneous addition of compliant and stiff phases where each contributes its inherent characteristics to produce optimum stiffness, strength and toughness. Previous works on such hybrid composites [18–20] have shown enhanced fracture toughness and energy absorption. In the recent years, a number of polyol based reactive diluents has been considered as a good choice for improving the fracture resistance of brittle epoxies [20,21]. In addition to the toughening effect, the lower viscosity and the extended pot life of polyols generally increase the level of filler loading as well as the resin wetting action without a substantial decrease in curing rate and thermal stability. These properties make polyols suitable for modification of epoxy resins to achieve improved peel and impact strengths, and facilitate processing of particle-filled and fiber-reinforced PMCs. For instance, the use of polyether polyol as a toughener for epoxy resins by Isik et al. [20] provided 160% enhancement in impact strength. In the past few decades, researchers have also successfully tailored the matrix properties by using nanofillers [22]. Since their discovery in 1991 by Iijima [23], carbon nanotubes (CNTs) have emerged as potential candidates for matrix modification because of their exceptional strength and stiffness [24], flexibility, diameter dependent specific surface area and high aspect ratio with low density [25]. These remarkable features of CNTs make them to act as bridges between crack faces and induce interlocking with the matrix material. However, to incorporate CNTs as effective reinforcements, good dispersion and interfacial adhesion between matrix and CNTs is desirable. Previously, it has been

* Corresponding author. Tel.: +1 334 844 3327; fax: +1 334 844 3307.
E-mail addresses: jajamkc@auburn.edu (K.C. Jajam), tippuhv@auburn.edu (H.V. Tippur).

1359-835X/$ - see front matter © 2014 Elsevier Ltd. All rights reserved.
http://dx.doi.org/10.1016/j.compositesa.2013.12.014

shown that surfactant treatment and amino-functionalization of CNTs enhance their dispersibility in the epoxy matrix [26–30]. Furthermore, multi-walled carbon nanotubes (MWCNTs) exhibit better dispersion than single walled carbon nanotubes (SWCNTs) because of lower specific surface area in the former than the latter. Considering these features of polyols and CNTs, the authors [31] have recently processed and characterized epoxy composites modified with reactive polyol diluents and randomly-oriented amino-functionalized multi-walled carbon nanotubes (NH_2-MWCNTs).

Nanocomposites modified with CNTs as reinforcements in polymer matrices have been extensively investigated over the years [25,32]. The dispersion of 0.1 wt.% of amino-functionalized double-wall carbon nanotubes (DWCNTs) in epoxy using a calandering technique by Gojny et al. [33] resulted in improved tensile strength, Young's modulus and quasi-static fracture toughness. A thermo-mechanical study by Fidelus et al. [34] showed 70% improvement in tensile impact strength at 0.5 wt.% of randomly oriented MWCNTs in epoxy resin. In an another thermo-mechanical investigation, Zhou et al. [35] noted 90% improvement in storage modulus and an optimum flexural strength with 0.3 wt.% MWCNT/epoxy system. Seyhan et al. [36] used 3-roll milling to disperse CNTs into vinyl-ester-polyester hybrid resin. They found that nanocomposites containing MWCNTs and NH_2-MWCNTs exhibited higher tensile modulus, fracture toughness and fracture energy values relative to DWCNTs and NH_2-DWCNTs counterparts. Hsieh et al. [37] noted improved tensile, fracture and fatigue performances with increasing MWCNTs content in an anhydride-cured epoxy. Some efforts to enhance the fracture toughness of CNT/epoxy nanocomposites by simultaneous addition of a third phase filler such as rubber and/or nanosilica particles have also been made [38,39].

While numerous studies have been reported on plasticized epoxies and/or CNT reinforced nanocomposites, they mostly deal with material processing aspects, thermo-mechanical characterization, and are limited to fracture behavior under quasi-static loading conditions. A few works, however, have addressed dynamic fracture behavior of nano-size spherical particle-filled nanocomposites. For example, Shukla et al. [40] and Evora et al. [41,42] reported improved fracture toughness and higher crack velocities in TiO_2 (35 nm) and Al_2O_3 (14 nm) nanoparticle filled composites relative to the neat resin. A recent study by Jajam and Tippur [16] on fracture behavior of particulate composites showed that PMCs are indeed loading rate dependent. They observed higher crack initiation toughness for nano-silica (20 nm) filled epoxies under quasi-static loading when compared to low velocity impact loading while both showed improvement relative to unfilled epoxy. Note that much of the published research to date on fracture behavior of nanocomposites has been performed quasi-statically and very limited data exists from the perspective of dynamic crack growth caused by rapid loading. Further, the reported ones primarily deal with low aspect ratio fillers. Higher aspect ratio of stiff fillers in conjunction with plasticizers, however, could vary the mechanical response in general and fracture behavior in particular. To the best of authors' knowledge, no study on dynamic fracture related to the combined effect of CNTs and plasticizers on epoxy system, has yet been documented in the literature. These gaps need to be bridged if such materials are to find engineering applications where stress-wave loading conditions dominate. Thus, the objective of the present research is to study fracture behavior of epoxy composites modified with reactive polyol diluent and randomly-oriented amino-functionalized MWCNTs under dynamic loading conditions. The loading rate effects and synergistic characteristics of NH_2-MWCNTs and polyether polyol on epoxy resin system are of particular interest.

2. Materials processing and characterization

2.1. Materials

A low viscosity epoxy system (Applied Poleramics Inc., USA) consisting of unmodified diglycidylether of bisphenol-A (DGEBA) resin cured by cycloaliphatic amine hardener was used as the matrix. An epoxy terminated polyether polyol (triglycidyl ether of propoxylated glycerin) (Applied Poleramics Inc., USA) was used as a reactive diluent and toughener. The amino-functionalized multi-walled carbon nanotubes (NH_2-MWCNTs) synthesized by catalytic chemical vapor deposition (purity > 95%, average diameter ~10 nm, average length ~1 μm) received from Nanocyl, Belgium, were used as stiff fillers.

2.2. Composites manufacturing process

Four categories of samples were prepared in this study: neat epoxy, epoxy/CNT(0.3 wt.%), epoxy/polyol(10 phr) and hybrid epoxy/CNT(0.3 wt.%)/polyol(10 phr). Table 1 presents the sample codes and formulations of all the epoxy composites used in this work. The choice of 0.3 wt.% NH_2-MWCNTs and 10 phr polyol was based on previous studies [31,43] that offered optimum gain in mechanical properties.

For EP–CNT system, the 0.3 wt.% NH_2-MWCNTs were dispersed in unmodified DGEBA resin at room temperature using a sonicator probe at 35% amplitude and a 30 s 'on'/30 s 'off' cycle in pulse mode for 1 h. To overcome the increase in pressure and temperature, the mixture was kept in a cooling bath during sonication. For effective dispersion of CNTs, the sonicated mixture was subsequently subjected to a three-roll shear mixing process, as shown schematically in Fig. 1. The rollers 1 and 3 rotate in the same direction and opposite to the middle roller 2 thereby inducing shear to the mixture. A gap setting between the rollers of 20 μm (1st pass), 10 μm (2nd pass) and 5 μm (3rd pass) was used to induce a high degree of shear to the mixture. The speed of the rollers was maintained at a ratio of 1:3:9 with a maximum speed of 200 rpm in all the three passes.

A conventional mechanical mixing technique was used to prepare EP–POL system by blending 10 phr polyol into the unmodified epoxy resin. For hybrid EP–CNT–POL system, 0.3 wt.% NH_2-MWCNTs were dispersed in 10 phr polyol modified epoxy resin using sonication and three-roll shear mixing process described above. The schematic shown in Fig. 1 depicts the manufacturing process for polyol modified epoxy (EP–POL) and epoxy/NH_2-MWCNTs/polyol (EP–CNT–POL) hybrid composites.

Table 1
Formulation of neat and modified epoxy samples.

Sample nomenclature	DGEBA[a] (phr)	Polyol content (phr)	NH_2-MWCNTs content (wt.%)
EP (neat epoxy)	100	0	0
EP–CNT (Epoxy + NH_2-MWCNT)	100	0	0.3
EP–POL (Epoxy + Polyol)	90	10	0
EP–CNT–POL (Epoxy + NH_2-MWCNT + Polyol)	90	10	0.3

[a] The hardener content was 30 phr for all formulations.

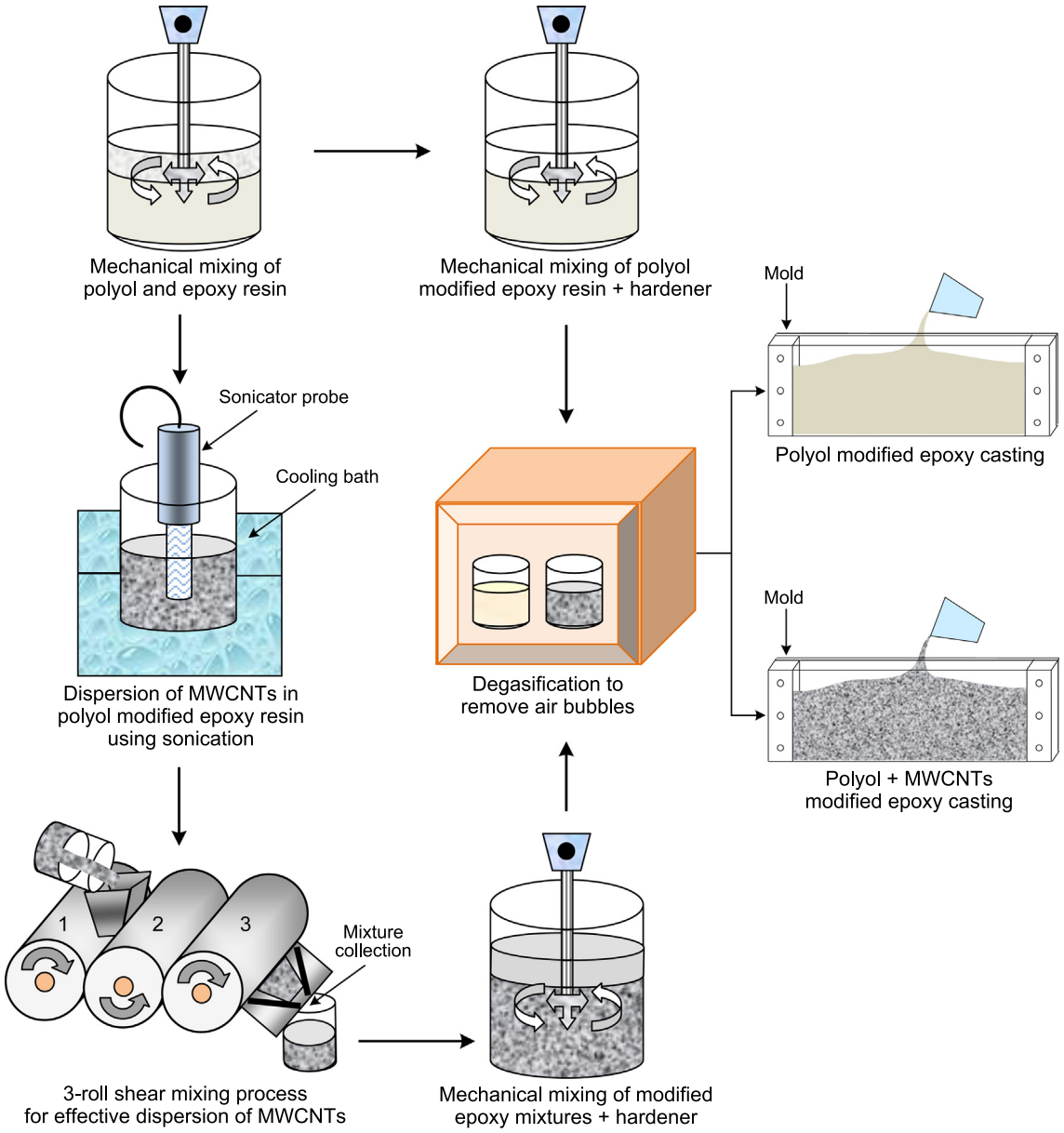

Fig. 1. Schematic of the manufacturing process for modified epoxy composites. (For interpretation of the references to color in this figure legend, the reader is referred to the web version of this article.)

The stoichiometric amount of the hardener was added to the neat and modified resin systems and blended using a mechanical stirrer for 10 min. The resulting blends were subjected to degasification to remove any trapped bubbles generated during mixing. After degassing, the mixtures were poured into molds coated with a release-agent and cured for 2 h at 60 °C followed by post curing at 100 °C for 5 h. The composite sheets were further rested at room temperature for a week prior to machining and testing.

2.3. Microstructural characterization

The quality of CNTs dispersion in the modified epoxies was examined using a ZEISS EM10 transmission electron microscope (TEM) at an accelerating voltage of 60 kV. Figs. 2(a) and (b) show the quality of dispersion of CNTs in EP–CNT and EP–CNT–POL samples, respectively, manufactured using sonication and 3-roll shear mixing process. The low magnification TEM image in Fig. 2(b) shows the morphology of the hybrid material with relatively well-dispersed CNTs and polyol domains along with a presence of few small CNTs agglomerates. The fractured surfaces (to be discussed later) were studied using a scanning electron microscope (SEM).

2.4. Elastic characterization

The dynamic elastic characteristics of all the samples were evaluated by indirect means using ultrasonic pulse-echo [44] measurement averaged at several discrete locations of the cured sheets. The longitudinal (C_L) and shear (C_S) wave speeds were determined by measuring transit time for the elastic pulse to travel twice the thickness of the sample using 10 and 5 MHz transducers, respectively. The mass density, ρ, of each composition was also determined. The values of dynamic elastic modulus (E_d) and Poisson's ratio (ν_d) were then calculated using measured wave speeds and density using,

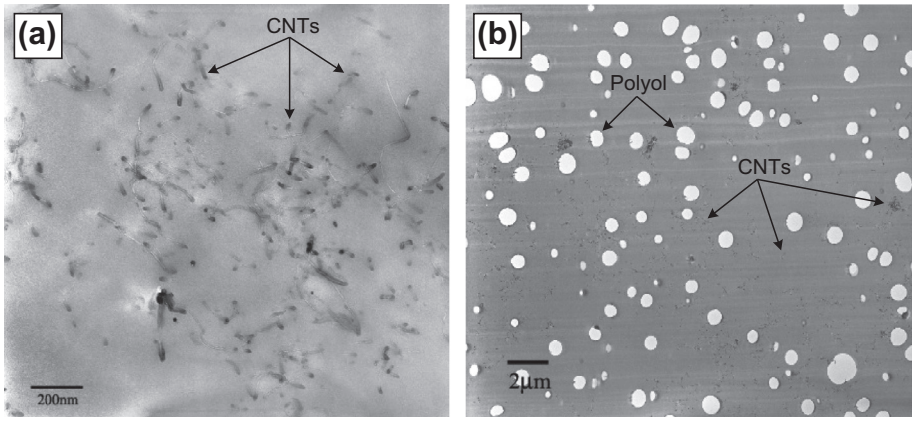

Fig. 2. (a) TEM micrograph showing CNTs dispersion in EP–CNT sample, (b) low magnification TEM image of CNTs and polyol dispersion in EP–CNT–POL system.

$$C_L = \sqrt{\frac{E_d(1-\nu_d)}{\rho(1+\nu_d)(1-2\nu_d)}}, \quad C_S = \sqrt{\frac{E_d}{2\rho(1+\nu_d)}}. \tag{1}$$

The values of Poisson's ratio in these composites were found to be nearly constant at 0.353 ± 0.011. The measured wave speeds (C_L and C_S) and the dynamic elastic modulus (E_d) for all samples are shown in Fig. 3. It can be seen that the epoxy composites show only modest changes in C_L, C_S and E_d relative to the neat epoxy.

2.5. Specimen fabrication and geometry

The cured composite sheets were machined into rectangular specimens of nominal dimensions 100 mm × 12.5 mm × 5 mm for quasi-static fracture tests (span 60 mm) and 212 mm × 50 mm × 8 mm for dynamic fracture experiments (span 196 mm) as shown in Figs. 4(a) and (b), respectively. An edge notch of 3 mm and 10 mm in length was first cut using a diamond impregnated wafer blade (thickness ~300 μm) into the samples for quasi-static and dynamic fracture tests, respectively. The notch tip was manually sharpened using a razor blade to achieve a consistent crack initiation followed by a steady growth [45].

The dynamic fracture experiments were performed using the method of digital image correlation (DIC) to quantify crack-tip deformations and hence the crack growth parameters. To facilitate this, a stochastic speckle pattern was created on the specimen surface by spraying a fine mist of black and white paints successively. Fig. 4(b) depicts the specimen geometry and loading configuration along with the crack tip coordinate system used for data analysis with an illustration of random speckle pattern. The dotted box represents 30 × 30 mm^2 region-of-interest.

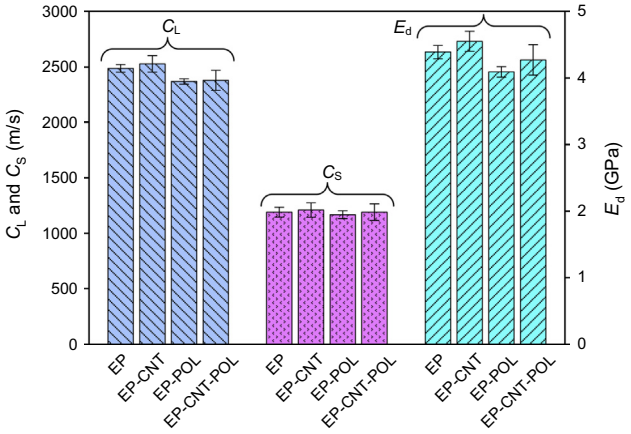

Fig. 3. Measured dynamic material properties using ultrasonic pulse-echo method. (EP: neat epoxy, EP–CNT: epoxy/CNT, EP–POL: epoxy/polyol, EP–CNT–POL: epoxy/CNT/polyol). (For interpretation of the references to color in this figure legend, the reader is referred to the web version of this article.)

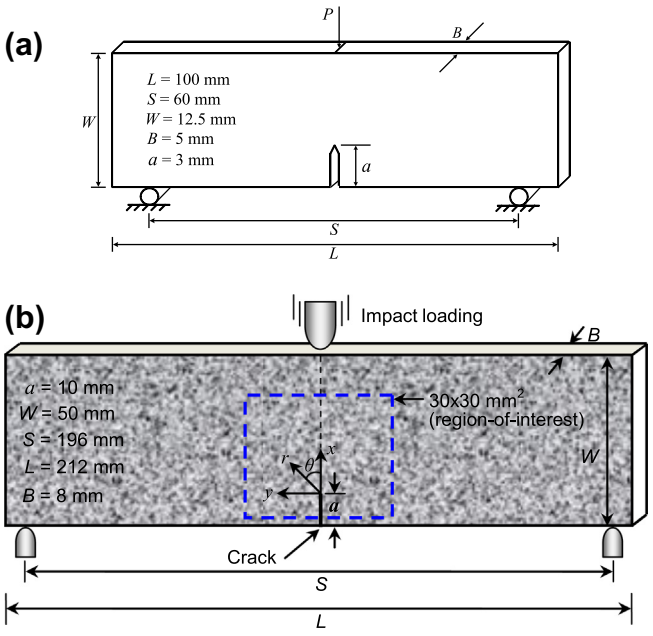

Fig. 4. Specimen geometry and loading configurations: (a) quasi-static fracture, and (b) dynamic fracture. (For interpretation of the references to color in this figure legend, the reader is referred to the web version of this article.)

3. Experimental details

3.1. Quasi-static fracture tests

Single edge notch bend (SENB) tests were conducted to measure quasi-static crack initiation toughness, K_{Ic}, according to ASTM D5045 standard [46]. The SENB specimens were loaded in a displacement control mode (crosshead speed = 0.2 mm/min) and symmetric three point bending configuration using an Instron 4465 testing machine. Typically, five specimens were tested for each of the four categories. The load-deflection data was recorded up to complete fracture and K_{Ic} was calculated using the load at initiation and specimen geometry using [47]

$$K_{Ic} = \frac{3\frac{PS}{BW^2}\sqrt{a}}{2\left(1+2\frac{a}{W}\right)\left(1-\frac{a}{W}\right)^{3/2}} \times \left[1.99 - \frac{a}{W}\left(1-\frac{a}{W}\right)\left\{2.15 - 3.93\left(\frac{a}{W}\right) + 2.7\left(\frac{a}{W}\right)^2\right\}\right] \quad (2)$$

where P, S, B, W and a are the load at fracture, span, thickness, width and crack length of the specimen, respectively (Fig. 4(a)).

3.2. Dynamic fracture tests

3.2.1. Experimental setup and testing procedure

The optical method of 2D DIC coupled with high-speed photography was used to study dynamic fracture behavior by measuring crack tip deformations in real-time. The details regarding DIC approach and the associated image analysis can be found in Refs. [45,48]. Briefly, in this method, the speckle patterns on a specimen surface in the region-of-interest were recorded before and during deformation. The speckle images from the deformed and reference states were correlated and the two in-plane orthogonal displacement fields were extracted.

The schematic of the experimental setup used is shown in Fig. 5. It consisted of a drop-tower (Instron-Dynatup 9250HV) for delivering low-velocity impact (impact velocity ≃4.5 m/s, mass = 5 kg) and a high-speed digital framing camera (Cordin 550) for recording the fracture event in real-time. The drop-tower was equipped with an instrumented tup (hemispherical profile, 25.4 mm diameter) and a pair of instrumented anvils for recording force and support reaction histories. The high-speed camera records images on 32 individual 1000 × 1000 pixel CCD sensor array positioned circumferentially around a five-facet rotating mirror which reflects and sweeps light over these sensors (see Ref. [45] for optical details). The setup also included instrumentation to produce a delayed trigger pulse when the impactor contacted the specimen. In view of the short duration transient event, two high-energy flash lamps, triggered by the camera and a pulse generator, were used to illuminate the specimen surface. Also, two separate computers, one to record the impact force and anvil reaction histories, and the other to control the high-speed camera and to store the images were used.

As shown in Fig. 5, the specimen decorated with random speckles was initially rested on two instrumented anvils and the camera was focused on a 30 × 30 mm^2 region-of-interest in the crack tip vicinity. Prior to impacting the specimen, a set of 32 reference images (undeformed set) were recorded at a framing rate of 250,000 frames per second. While keeping the camera settings the same, a second set of 32 images (deformed set) was captured when the specimen was impacted. A total of 32 images were recorded with a 4 μs interval between successive images for each undeformed and deformed sets. The corresponding images recorded by each of the sensors were paired and analyzed to get crack-opening and crack-sliding displacement fields.

3.2.2. Evaluation of crack velocity and stress intensity factors

Each speckle image from the deformed set was digitized to locate the current position of the crack tip. Subsequently, the crack velocity (V) was estimated from the crack length history [49].

A sub-image size of 26 × 26 pixels (1 pixel = 30 μm on the specimen) was chosen for correlation without any overlap to generate 37 × 37 displacement vector grids for both crack-opening (v) and crack-sliding (u) displacement fields. The mode-I and mode-II stress intensity factors (SIFs) were evaluated using an over-deterministic least-squares analysis [50] of displacement fields. The governing asymptotic expression for u and v fields near the tip of a steadily growing crack is given by [51],

$$\begin{Bmatrix} u(r,\theta) \\ v(r,\theta) \end{Bmatrix} = \sum_{n=1}^{\infty} \frac{\left(K_I^d\right)_n B_I(V)}{2\mu}\sqrt{\frac{2}{\pi}}(n+1) \times \begin{Bmatrix} r_1^{n/2}\cos\frac{n}{2}\theta_1 - h(n)r_2^{n/2}\cos\frac{n}{2}\theta_2 \\ -\beta_1 r_1^{n/2}\sin\frac{n}{2}\theta_1 + \frac{h(n)}{\beta_2}r_2^{n/2}\sin\frac{n}{2}\theta_2 \end{Bmatrix} + \sum_{n=1}^{\infty} \frac{\left(K_{II}^d\right)_n B_{II}(V)}{2\mu}\sqrt{\frac{2}{\pi}}(n+1) \times \begin{Bmatrix} r_1^{n/2}\sin\frac{n}{2}\theta_1 - h(\bar{n})r_2^{n/2}\sin\frac{n}{2}\theta_2 \\ \beta_1 r_1^{n/2}\cos\frac{n}{2}\theta_1 + \frac{h(\bar{n})}{\beta_2}r_2^{n/2}\cos\frac{n}{2}\theta_2 \end{Bmatrix} \quad (3)$$

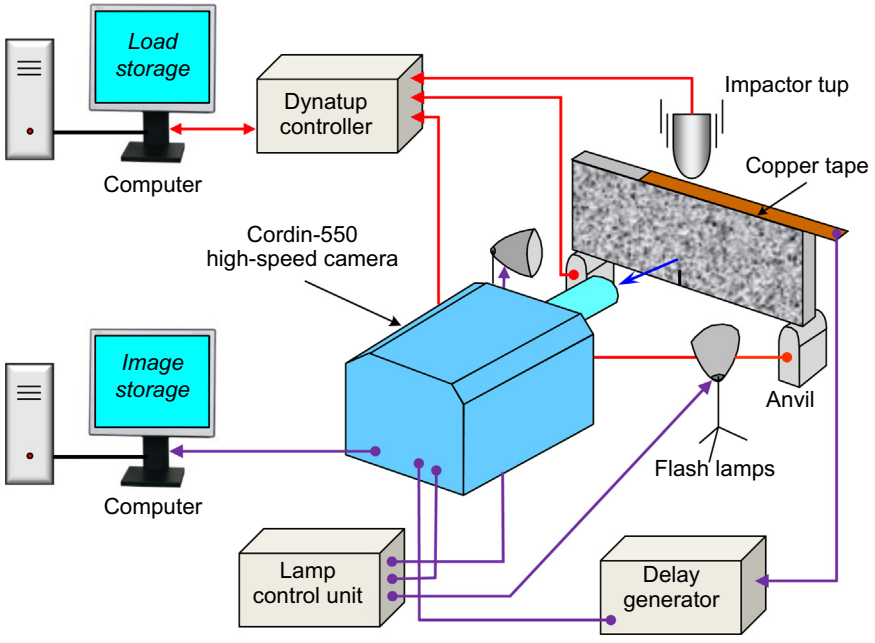

Fig. 5. Schematic of the experimental setup for dynamic fracture study using digital image correlation and high-speed photography. (For interpretation of the references to color in this figure legend, the reader is referred to the web version of this article.)

where

$$r_m = \sqrt{x^2 + \beta_m^2 y^2}, \quad \theta_m = \tan^{-1}(\beta_m y/x), \quad m = 1, 2,$$
$$\beta_1 = \sqrt{1 - (V/C_L)^2}, \quad \beta_2 = \sqrt{1 - (V/C_S)^2}$$

$$C_L = \sqrt{\frac{(\kappa+1)\mu}{(\kappa-1)\rho}},$$
$$C_S = \sqrt{\frac{\mu}{\rho}}, \kappa = (3 - \nu_d)/(1 + \nu_d) \text{ for plane stress}$$

$$h(n) = \begin{cases} 2\beta_1\beta_2/(1+\beta_2^2) : n \text{ odd} \\ (1+\beta_2^2)/2 : n \text{ even} \end{cases} \quad \text{and} \quad h(\bar{n}) = h(n+1)$$

$$B_I(V) = \frac{(1+\beta_2^2)}{D}, \quad B_{II}(V) = \frac{2\beta_2}{D}, \quad D = 4\beta_1\beta_2 - (1+\beta_2^2)^2. \qquad (4)$$

In the above equations, (r, θ) and (x, y) are the instantaneous polar and Cartesian coordinates, respectively, defined at the current crack tip, V is the crack tip velocity, C_L and C_S are longitudinal and shear wave speeds of the material, ρ is the mass density, μ and ν_d are the dynamic shear modulus and the Poisson's ratio, respectively. The coefficients $\left(K_I^d\right)_n$ and $\left(K_{II}^d\right)_n$ of the dominant terms ($n = 1$) are the mode-I and mode-II dynamic SIFs, respectively. In order to extract SIF history, a number of data points were collected in the vicinity of the current crack tip $0.4 < r/B < 1.5$ (B is the specimen thickness) and $(-150° \leqslant \theta \leqslant -90°$ and $90° \leqslant \theta \leqslant 150°)$ to minimize triaxial effects on least-squares method using analytical expressions based on a 2D analysis in Eq. (3). Note that Eq. (3) can be reduced to the form of a dynamically loaded stationary crack in the limit the crack velocity $V \to 0$ and was used to extract SIF history prior to crack initiation.

4. Results and discussion

4.1. Quasi-static fracture response

The quasi-static fracture response of neat epoxy and modified epoxy composites is shown in Fig. 6. Typical load-deflection curves of all formulations are shown in Fig. 6(a). It can be seen that the load rises linearly for neat epoxy (EP) and epoxy/CNT (EP–CNT) systems whereas the epoxy/polyol (EP–POL) and epoxy/CNT/polyol (EP–CNT–POL) composites show a degree of nonlinear behavior in the initial as well as in the intermediate stages of deformation. Except for neat epoxy, a noticeable nonlinearity is seen in all specimens prior to fracture at which abrupt crack growth ensues causing a sudden drop in the recorded load. Note that the peak loads and the corresponding load-point deflections at break increase after individual as well as simultaneous addition of NH_2-MWCNTs and polyol phases into epoxy. The incorporation of NH_2-MWCNTs as the stiff and polyol as the compliant phase results in increasing and decreasing slopes of the load-deflection curves, respectively, relative to the neat epoxy, whereas the hybrid system containing both stiff and compliant phases show lower stiffness than the EP–CNT system but higher than the EP and EP–POL counterparts. Further, note that the work needed for crack initiation (area under the load-deflection curve) is the maximum for hybrid EP–CNT–POL system among all the compositions.

The measured quasi-static crack initiation toughness (K_{Ic}) values for all formulations are shown in Fig. 6(b). Each data represents an average of five measured values of K_{Ic} and the error bars indicate standard deviations. A significant enhancement in the quasi-static fracture property is quite evident in each modified epoxy system. With respect to neat epoxy, the gain in K_{Ic} values

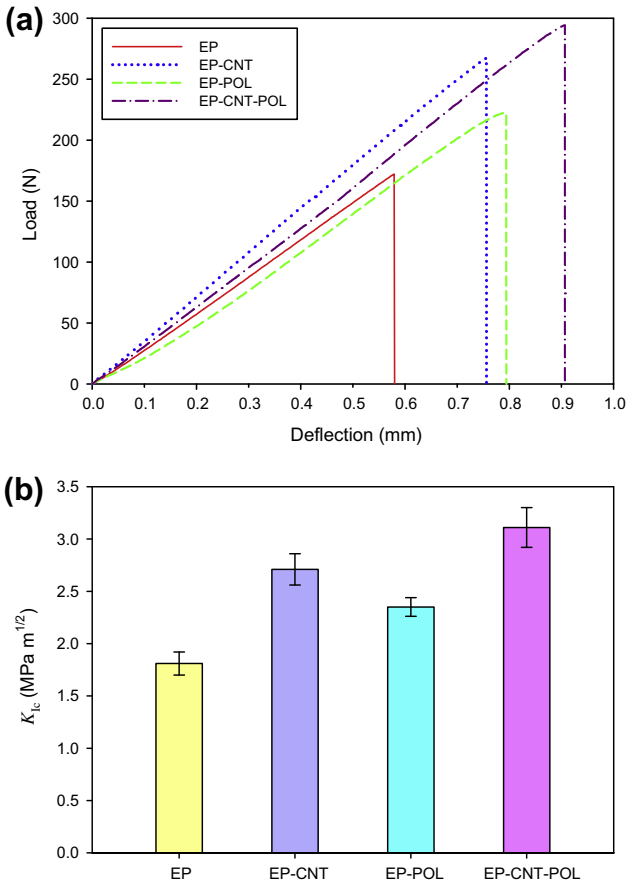

Fig. 6. Mode-I quasi-static fracture tests: (a) typical load-deflection responses, and (b) quasi-static crack initiation toughness (K_{Ic}) of different formulations. (For interpretation of the references to color in this figure legend, the reader is referred to the web version of this article.)

for EP–CNT and EP–POL systems are ~50% and ~30%, respectively, indicating that the 0.3 wt.% addition of NH_2-MWCNTs is more effective than the 10 phr polyol as a toughener. However, the simultaneous incorporation of both phases offers the maximum improvement of ~70% in K_{Ic} value for the hybrid EP–CNT–POL system relative to the neat epoxy. The synergistic effect of stiffening the epoxy with CNTs while toughening with polyol seems to yield the best outcome.

4.2. Dynamic fracture behavior

4.2.1. Experimental repeatability

Due to the transient nature of deformation at elevated loading rates, multiple experiments were first performed in order to verify repeatability in the fracture behavior, and hence, the crack growth measurements. Fig. 7 shows the repeatability of dynamic fracture experiments in terms of the impact force, crack length and mode-I SIF histories for hybrid EP–CNT–POL composites. The tup and anvil load histories are shown in Fig. 7(a) for the four EP–CNT–POL specimens. (Note that the tup forces are shown as positive instead of negative.) An excellent repeatability in the tup force as well as in the left and right support reaction histories is self evident. In these experiments, the complete fracture of the specimen occurred within ~225 μs after impact. Thus, only the dominant first peak of the tup force history is significant. Note that the supports register reaction force after ~300 μs by which time the crack propagates the entire specimen width. Hence, the reaction forces from support anvils do not contribute to the crack initiation and growth in these specimens, suggesting that a free-free cracked

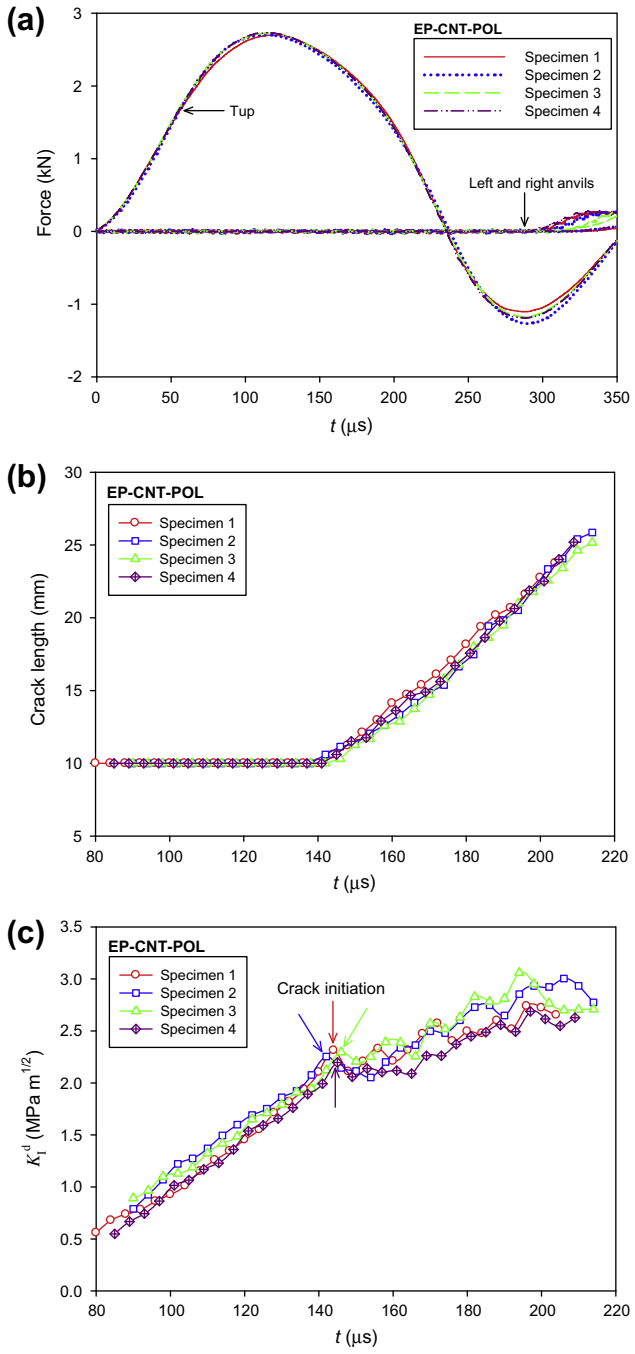

Fig. 7. Repeatability of dynamic fracture experiments for EP–CNT–POL specimens: (a) impactor force and support reaction histories, (b) crack length histories, and (c) mode-I dynamic SIF (K_I^d) histories. (For interpretation of the references to color in this figure legend, the reader is referred to the web version of this article.)

beam model should suffice analytical or computational simulation of these experiments.

The crack length histories for the same set of specimens are plotted in Fig. 7(b). Prior to impact, the specimens had a crack (pre-notch) length of 10 mm. When the impactor contacted the specimen ($t = 0$), the compressive stress waves propagated the specimen width and took 142–146 μs to initiate the crack. After loading, the compressive stress waves reflect back as tensile waves from the specimen edge opposite to the impact edge, initiating the crack tip in a mode-I fashion. Following initiation, a repeatable and monotonic crack growth is evident in all specimens until complete fracture with minor deviations in the crack length due to the highly transient nature of failure.

The mode-I dynamic SIF (K_I^d) histories for EP–CNT–POL composites are shown in Fig. 7(c). The K_I^d value at crack initiation is indicated by an arrow for each specimen. The SIF increases monotonically until crack initiation, followed by a noticeable drop in K_I^d values for all specimens due to elastic unloading. This is accompanied by a gradual increase in K_I^d values until the complete fracture of the specimens. It is important to note that from the perspective of dynamic fracture experiments, the K_I^d profiles show a very good repeatability throughout the fracture event.

4.2.2. Dynamic crack growth responses

A few representative speckle images and the corresponding crack-opening (v-field or displacement along the y-axis) and crack-sliding (u-field or displacement along the x-axis) displacement contours for each sample category are presented in Fig. 8. Each speckle image represents 30×30 mm^2 region-of-interest recorded by the high-speed camera where surface deformations were monitored optically. The specimens were subjected to symmetric impact loading and the initial notch as well as the sharp growing crack is visible as indicated by the arrows. In order to compare the extent of crack growth, the speckle images for each formulation are selected at a particular time instant, $t = 158$ μs. It can be seen that at this time instant, the crack extension in neat epoxy and epoxy/CNT specimens is nearly equal and larger than the epoxy/polyol and hybrid epoxy/CNT/polyol counterparts. As described earlier, a sub-image size of 26×26 pixels was chosen for image correlation analysis and displacement fields were obtained as a 37×37 array of data points for each time instant. Subsequently, full-field displacement contours with 5 μm per contour increment were generated. The crack-opening and crack-sliding displacement fields show that contour lines are nearly symmetric relative to the crack, consistent with a dominant mode-I fracture behavior. The crack-sliding displacement field shows a set of isolines emerging from the right side of the contour plots due to impact loading.

A comparison of dynamic fracture performance in terms of the transient load, crack length and SIF histories for all formulations of modified epoxy composites is made in Fig. 9. The tup force and anvils reactions experienced by each type of composite are compared in Fig. 9(a). The peak impact force (compressive) recorded by the piezoelectric tup in case of epoxy/CNT (EP–CNT) system is the maximum indicating higher contact stiffness and peak impact load among all the cases. The hybrid epoxy/CNT/polyol (EP–CNT–POL), neat epoxy (EP) and epoxy/polyol (EP–POL) composites exhibit decreasing trends, successively. However, the dominant peak duration is slightly longer for EP–POL and EP–CNT–POL cases than the EP and EP–CNT counterparts due to a higher crack growth resistance in the former than the latter cases. The left and right anvil support reactions on the other hand do not register significant values until 300 μs causing a free-free beam condition to prevail during fracture in all the cases.

The instantaneous crack length histories for all samples are plotted in Fig. 9(b). The crack initiation occurred much later in the epoxy/CNT (118 μs), epoxy/polyol (144 μs) and hybrid epoxy/CNT/polyol (146 μs) composites when compared to the neat epoxy (98 μs). Following initiation and rapid acceleration (due to sudden release of energy from the initial crack tip), it can be seen that crack growth is essentially continuous in each case during the observation window. In each sample category, minimal deviations can be noted in the crack growth behavior due to the transient nature of stress wave dominant fracture. The slope of crack length histories was used to estimate crack tip velocity and are 325, 313, 210, 227 m/s for neat epoxy, epoxy/CNT, epoxy/polyol, epoxy/CNT/polyol composites, respectively as listed in Fig. 9(b). The crack growth

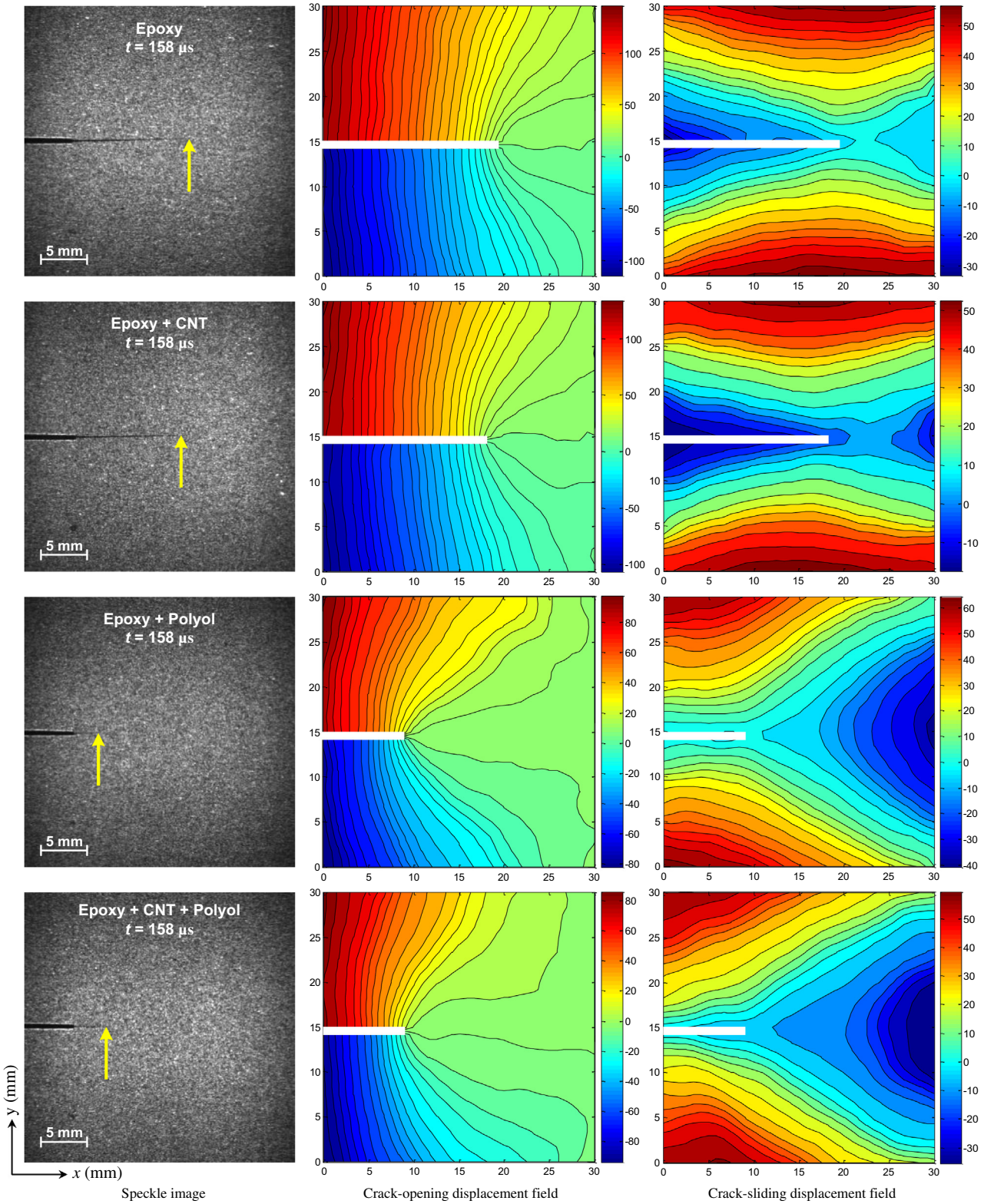

Fig. 8. Measured crack-opening and crack-sliding displacement fields at a time instant t = 158 μs corresponding to speckle images (first column) in 30 × 30 mm^2 region-of-interest. The arrows indicate the instantaneous crack tip position in the speckle images. Color bars represent displacement in μm. Contours are plotted in 5 μm increments. (For interpretation of the references to color in this figure legend, the reader is referred to the web version of this article.)

characteristics suggest that the addition of compliant phase (polyol) significantly retards the crack propagation in polyol modified composites.

The optically measured dynamic mode-I ($K_{\mathrm{I}}^{\mathrm{d}}$) and mode-II ($K_{\mathrm{II}}^{\mathrm{d}}$) SIF histories are shown in Fig. 9(c). Here t_{i} denotes the time at crack initiation after impact and the time base is shifted such that t–t_{i} = 0

corresponds to crack initiation as shown by the vertical dotted line, and hence the negative and positive values represent the pre-initiation and post-initiation periods, respectively. In the pre-initiation regime (t–t_i < 0), for each specimen the K_I^d increases monotonically until it reaches a threshold value at crack initiation. Following initiation, a noticeable drop in K_I^d can be seen and the maximum value of K_I^d just before the drop is identified as the mode-I dynamic crack initiation toughness, K_{Ii}^d. One can readily see that the magnitudes K_{Ii}^d show increasing trend with the addition of 0.3 wt.% NH_2-MWCNTs, 10 phr polyol and a combination of both into the epoxy matrix. Relative to neat epoxy (EP), the improvements in dynamic crack initiation toughness, K_{Ii}^d for EP–CNT, EP–POL and EP–CNT–POL composites are ~37%, ~65% and ~92%, respectively. The K_I^d values in the pre-initiation (t–t_i < 0) and post-initiation (t–t_i > 0) regimes are higher for EP–CNT, EP–POL and hybrid EP–CNT–POL composites when compared to that of neat epoxy. After crack initiation, the instantaneous values of K_I^d steadily rise but with an oscillatory behavior due to stress wave reflections in a finite size specimen. It should be noted that the mode-II dynamic SIF (K_{II}^d) values are close to zero throughout the failure event for each experiment, indicating a dominant mode-I fracture behavior.

The dynamic fracture performance of modified epoxy composites regarding crack initiation and crack growth parameters is quantified in Table 2. Each data is an average of 3–4 experiments, listed along with their standard deviation. The crack initiated in the polyol modified composites (EP–POL and EP–CNT–POL) at the same time range (142–146 μs) after impact and is longer than the initiation time needed for neat epoxy (98–102 μs) and epoxy/CNT (116–118 μs) samples indicating that the crack initiation can be significantly delayed with the incorporation of polyol phase. The maximum (V_{max}) and steady state (V_{ss}) crack velocities are lower for EP–POL and hybrid EP–CNT–POL composites relative to neat epoxy and EP–CNT samples suggesting higher crack growth resistance and dynamic crack initiation toughness in the former cases than the latter.

5. Loading rate effects and toughening mechanisms

In light of the experimental results discussed above, an obvious question that arises is, are the fracture behaviors of CNT and polyol modified epoxies loading rate dependent? Hence, it is instructive to compare fracture toughness at crack initiation for all cases under quasi-static and dynamic loading conditions. The role of loading rate on fracture parameters of these composites is presented in Fig. 10. In this work, the loading rate for a cracked specimen is defined as the rate of increase of SIF at crack initiation (quasi-static: $\dot{K}_I = dK_I/dt$; dynamic: $\dot{K}_I^d = dK_I^d/dt$) and determined experimentally for each type of composite from a linear fit of 4–5 data points prior to crack initiation. In Fig. 10, a systematic comparison is made between quasi-static and dynamic crack initiation toughness (K_{Ic} and K_{Ii}^d) for each material. The respective loading rate $\dot{K}_I$ and $\dot{K}_I^d$ values are listed for each composite as legends, and expressed in MPa$\sqrt{m}$/s. Again, each loading rate is an average of 3–5 experiments for each material category. Note that the dynamic loading rates ($\dot{K}_I^d$ values) are *six orders of magnitude greater* than the quasi-static ($\dot{K}_I$) counterparts. From Fig. 10, it can be seen that the fracture toughness values between quasi-static and dynamic cases differ from each other for the respective composites. At high loading rates ($\dot{K}_I^d \sim 10^4$ MPa$\sqrt{m}$/s), the crack initiation toughness values are lower than those corresponding to the quasi-static loading rates ($\dot{K}_I \sim 10^{-2}$ MPa$\sqrt{m}$/s). The difference is quite significant for EP–CNT composites, where the fracture toughness value for dynamic case is ~40% lower when compared to the quasi-static counterpart. However, the EP–POL system shows the least difference of ~17% between the toughness values among all the cases.

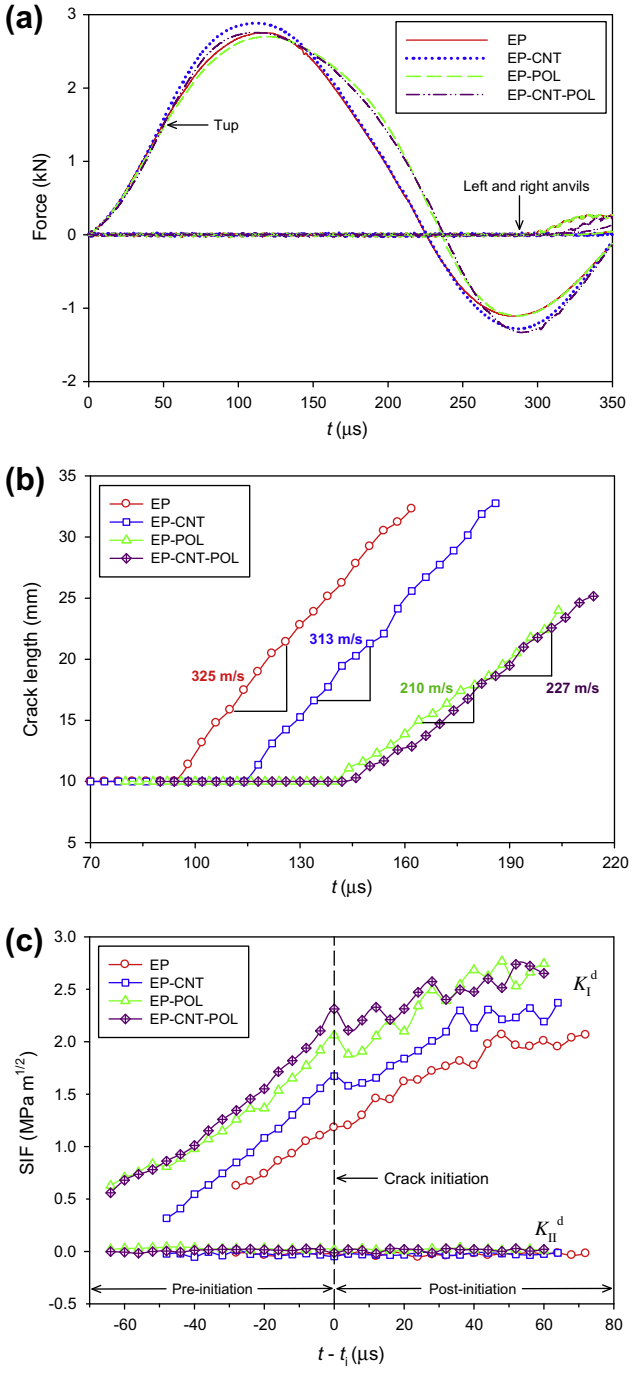

Fig. 9. Measured impact force and dynamic fracture parameter histories: (a) impact force and support reaction histories, (b) crack growth histories, and (c) dynamic SIFs (K_I^d and K_{II}^d) histories. (For interpretation of the references to color in this figure legend, the reader is referred to the web version of this article.)

Fractographic examination was used to study the toughening mechanisms under quasi-static and dynamic loading conditions. The SEM micrographs of quasi-statically fractured surfaces of neat and modified epoxy samples are shown in Fig. 11. A relatively smooth fracture surface with a presence of fine lines is seen in neat epoxy case as shown in Fig. 11(a) indicating a typical brittle and unstable crack growth behavior accounting for its low fracture toughness among all the cases. Figs. 11(b) and (c) depict the highly textured/rough surfaces for epoxy/CNT and epoxy/polyol composites, respectively. The roughness associated with the curved crack front/path indicates significant amount of inelastic deformation

Table 2
Measured dynamic fracture parameters for neat and modified epoxy samples.

Sample	Peak impact force (kN)	Crack initiation time, t (μs)	Maximum crack velocity, V_{max} (m/s)	Steady state crack velocity, V_{ss} (m/s)	Dynamic crack initiation toughness, K_{Ii}^{d} (MPa m$^{1/2}$)
EP	2.75 ± 0.08	98–102	442 ± 56	349 ± 23	1.18 ± 0.07
EP–CNT	2.88 ± 0.07	116–118	438 ± 44	323 ± 21	1.62 ± 0.06
EP–POL	2.64 ± 0.04	142–146	288 ± 10	214 ± 12	1.95 ± 0.11
EP–CNT–POL	2.71 ± 0.02	142–146	281 ± 12	219 ± 15	2.27 ± 0.05

and deviation of fracture planes from its original crack plane suggests highly interrupted and deflected crack paths requiring higher amounts of fracture energy. The fractured surface of hybrid epoxy/CNT/polyol composite shown in Fig. 11(d) appears to have a higher degree of roughness when compared to the other cases, and can be attributed to micro crack deflections and branched crack propagation in multiple planes caused by CNTs and immiscible polyol domains. The curved and vivid ridges can be seen throughout the fracture surface suggesting a cumulative contribution of nanotubes and polyol in the fracture toughness enhancement. As shown in Fig. 12, the micrograph for hybrid epoxy/CNT/polyol case shows uniformly dispersed spherical polyol domains and the presence of embedded CNTs is also visible in the magnified view of the highlighted region. The further magnified views of selected regions in the subsequent micrographs show matrix cracking through polyol domains along with the presence of pulled-out CNTs and CNT bridges at various locations on the fracture planes.

During fracture of CNTs modified epoxy nanocomposites, as the propagating matrix crack front encounters strong (11–63 GPa) and stiff (270–950 GPa) CNTs [24], crack face bridging occurs. Consequently, the bridging forces due to well-anchored nanotubes reduce the crack driving forces while absorbing additional fracture energy when CNTs are pulled-out. Further, crack front deceleration and frequent change in crack propagation planes also help dissipate more energy. In the case of polyol modified epoxies, the spherical polyol domains (Owing to the hydroxyl groups polyol has a tendency to react with DGEBA epoxy. However, it forms an immiscible phase with epoxy [20] and polyol phase separates during epoxy polymerization at 60 °C. This phase separation continues until complete polymerization of epoxy and diffusion of polyol molecules within the epoxy phase is inhibited. As the cure temperature increased to 100 °C, the immiscible phase might be diffusing into cured epoxy matrix leaving behind spherical polyol domains.) undergo inelastic deformation and considerable shear yielding, expected of ductile systems. Cavitation is another important factor in plasticizer toughened systems [20,52], and cavitation of polyol domains interrupts crack growth and causes shear deformation in the matrix. These are potentially the main sources of increased energy absorption and crack initiation toughness of polyol modified epoxy. In epoxy/CNT/polyol system, the above mechanisms of both modifiers (CNTs and polyol) act cooperatively to produce higher energy absorption.

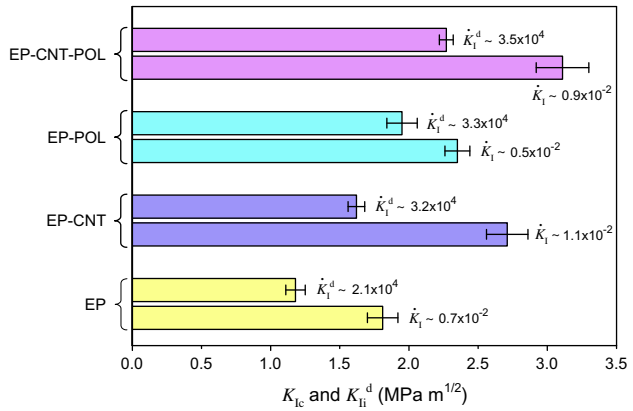

Fig. 10. Loading rate effects on mode-I crack initiation toughness of epoxy composites. (Quasi-static loading rate: $\dot{K}_I = dK_I/dt$; dynamic loading rate: $\dot{K}_I^d = dK_I^d/dt$. The $\dot{K}_I$ and $\dot{K}_I^d$ are expressed in MPa$\sqrt{m}$/s). (For interpretation of the references to color in this figure legend, the reader is referred to the web version of this article.)

The microscopic features of dynamically fractured surfaces are shown in Fig. 13 for each material. The broken arrows in these micrographs indicate the direction of crack propagation. The fractured surface of neat epoxy as shown in Fig. 13(a), reveals a relatively flat, smooth and featureless surface demonstrating its brittle nature with least energy expenditure among all the cases. In the case of epoxy/CNT composite, the micrograph in Fig. 13(b) shows that the surface roughness increased with the addition of CNTs into epoxy thereby forming the stepwise markings and cleavage planes. The magnified view in the inset shows CNT entanglements, pull-out as well as bridges. Fig. 13(c) illustrates the fracture surface of epoxy/polyol case showing inelastically deformed matrix with crack branches on various fracture planes. The finely distributed sub-micron size polyol domains can be observed in the inset along with the presence of micro cracks, riverbed markings and shear band features responsible for strain energy absorption. Fig. 13(d) shows the fracture surface of the hybrid epoxy/CNT/polyol composites. In addition to shear flow, deep furrows and higher cleavages are visible. The magnified view in the inset shows minor CNT agglomerates associated with dendriform cracks, acting as obstacles for the growing crack leading to deviation from its primary path thereby generating secondary cracks. The CNT pull-out, CNT bridges, matrix cracks, crack bifurcation and crack pining in polyol domains are the major toughening mechanisms in the case of hybrid composites.

With regards to loading rate effects, the micrographs shown in Figs. 11–13 reveal higher surface roughness and ruggedness for the quasi-static fractured specimens when compared to dynamic counterparts and accounts for the higher crack initiation toughness in the former cases. Note that the addition of polyols to epoxy increased the fracture energy due to higher ductility of the polyol domains. Additionally, CNTs have a high aspect ratio and possess flexible elastic behavior as well as strong interfacial bonding due to ammonia-functionalization, resulting in the nanophase resin systems exhibiting higher absorption of energy. Moreover, CNTs serve as effective crack bridges inducing mechanical interlocking with the matrix material. In addition to bridging, the strongly bonded CNTs significantly absorb fracture energy when pulled-out from the matrix. Moreover, CNTs also add to momentary crack arrest and/or deflection during propagation. These combined effects of both the fillers provide the greatest enhancement in crack initiation toughness in the hybrid composites.

6. Conclusions

In this work, the role of loading rate on fracture behavior of epoxy composites modified with reactive polyol diluent and randomly-oriented amino-functionalized multi-walled carbon nanotubes has been studied. The edge cracked composite samples were subjected

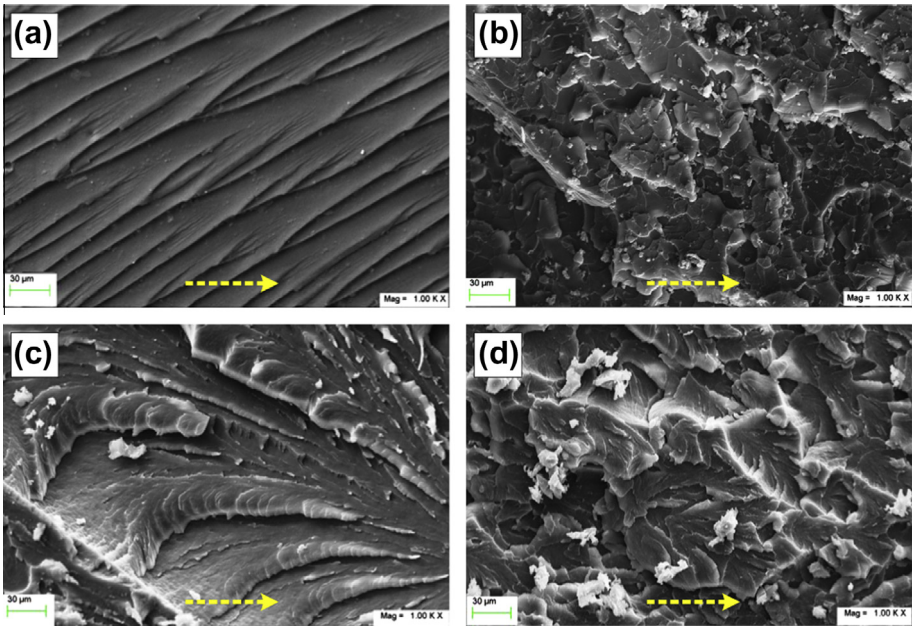

Fig. 11. SEM micrographs of quasi-statically fractured surfaces: (a) Epoxy, (b) Epoxy–CNT, (c) Epoxy–Polyol, and (d) Epoxy–CNT–Polyol. (The dotted arrow indicates the direction of crack propagation). (For interpretation of the references to color in this figure legend, the reader is referred to the web version of this article.)

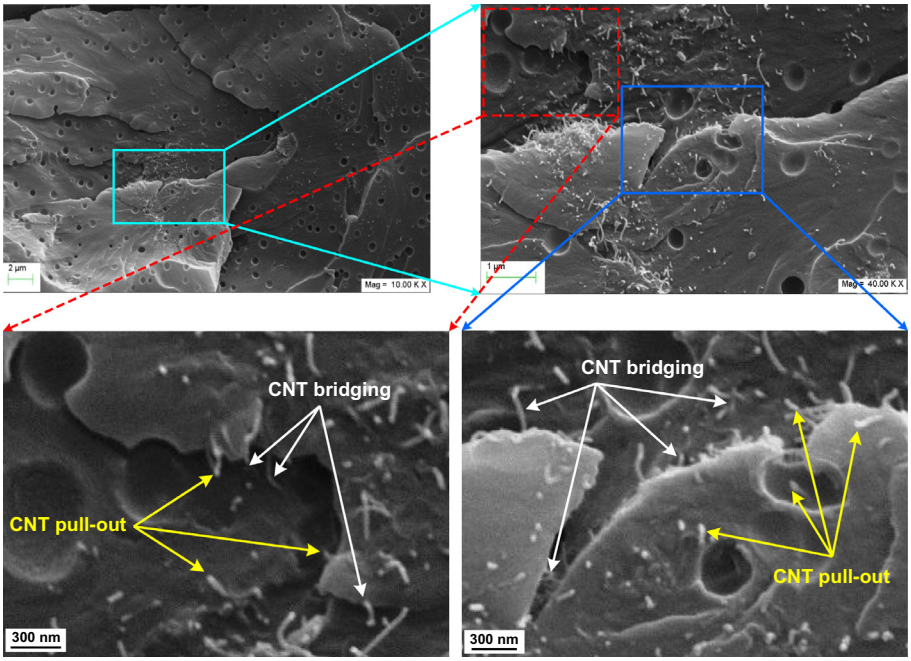

Fig. 12. SEM micrographs of quasi-static fracture surface of epoxy–CNT–Polyol hybrid composite showing CNT pull-out and CNT bridging. (For interpretation of the references to color in this figure legend, the reader is referred to the web version of this article.)

to quasi-static and dynamic fracture in symmetric loading configurations. The full-field optical method of 2D digital image correlation along with high-speed photography was used to evaluate dynamic fracture parameter histories. Fractographic examination was performed in order to understand the toughening behaviors. The major results of this study are summarized as follows:

- Ultrasonic pulse-echo measurements showed only minor differences in longitudinal (C_L), shear (C_S) wave speeds and dynamic elastic modulus (E_d) among neat epoxy, epoxy/CNT, epoxy/polyol and epoxy/CNT/polyol systems.
- A significant enhancement in the quasi-static crack initiation toughness (K_{Ic}) was observed in each modified system relative to neat epoxy. The K_{Ic} was the highest (~70% enhancement) for the hybrid epoxy/CNT/polyol system among all the four formulations.
- Dynamic fracture tests showed the lowest crack speed for epoxy/polyol and hybrid epoxy/CNT/polyol composites when compared to the neat epoxy and epoxy/CNT counterparts. The crack took significantly longer to initiate in epoxy/polyol and hybrid epoxy/CNT/polyol composites than neat epoxy and epoxy/CNT samples.

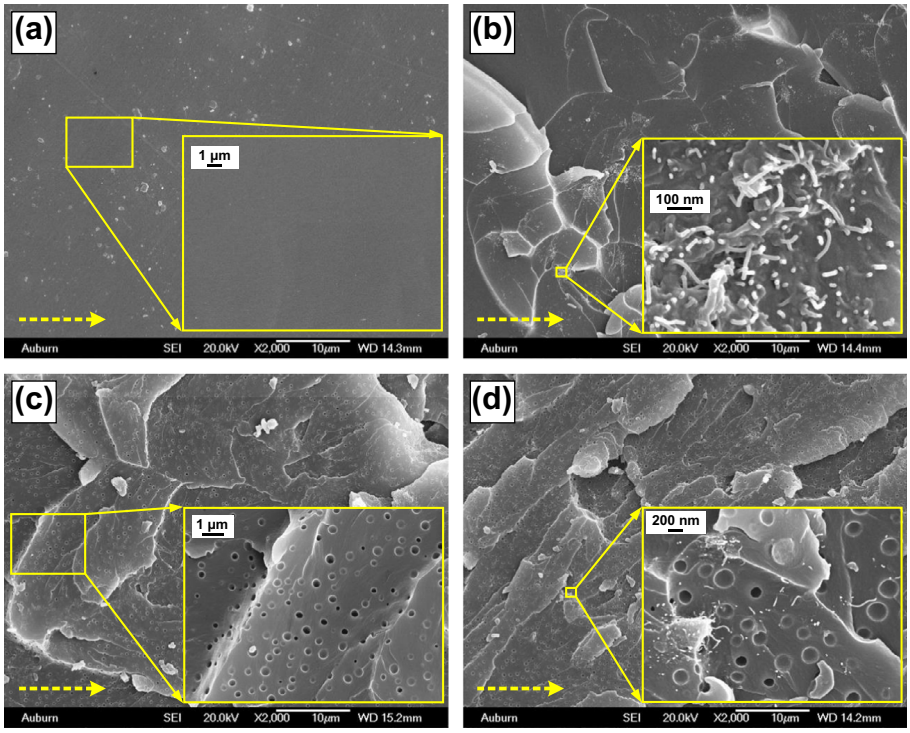

Fig. 13. SEM micrographs of dynamically fractured surfaces: (a) Epoxy, (b) Epoxy–CNT, (c) Epoxy–Polyol, and (d) Epoxy–CNT–Polyol. (The dotted arrow indicates the direction of crack propagation). (For interpretation of the references to color in this figure legend, the reader is referred to the web version of this article.)

- Relative to neat epoxy, the improvements in dynamic crack initiation toughness values for epoxy/CNT, epoxy/polyol and hybrid epoxy/CNT/polyol systems were ~37%, ~65%, and ~92%, respectively.
- The fracture behavior in these composites is loading rate sensitive. At high loading rates ($\dot{K}_I^d \sim 10^4$ MPa$\sqrt{m}$/s), the crack initiation toughness values were consistently lower relative to the quasi-static ($\dot{K}_I \sim 10^{-2}$ MPa$\sqrt{m}$/s) counterparts. The effect was more significant for epoxy/CNT composites, with dynamic crack initiation toughness value ~40% lower than the quasi-static value.
- The microscopic examination revealed a combination of toughening mechanisms including plastic deformation, crack deflection, CNT bridges and pull-outs. These features were more pronounced in quasi-static cases showing higher surface ruggedness compared to dynamic counterparts, accounting for higher crack initiation toughness in the former.

Acknowledgements

This research was sponsored by the NASA under EPSCoR Grant No. NNX10AN26A. The first author gratefully acknowledges the AL-EPSCoR GRSP Round-7 Fellowship from the Alabama Commission on Higher Education.

References

[1] Kinloch AJ, Shaw SJ, Tod DA, Hunston DL. Deformation and fracture behaviour of a rubber-toughened epoxy: 1. Microstruct Fract Stud Polym 1983;24(10):1341–54.
[2] Yee AF, Pearson RA. Toughening mechanisms in elastomer-modified epoxies. J Mater Sci 1986;21(7):2462–74.
[3] Ratna D. Phase separation in liquid rubber modified epoxy mixture. Relationship between curing conditions, morphology and ultimate behavior. Polymer 2001;42(9):4209–18.
[4] Kinloch AJ, Yuen ML, Jenkins SD. Thermoplastic-toughened epoxy polymers. J Mater Sci 1994;29(14):3781–90.
[5] Wong DWY, Lin L, McGrail PT, Peijs T, Hogg PJ. Improved fracture toughness of carbon fibre/epoxy composite laminates using dissolvable thermoplastic fibres. Compos A Appl Sci Manuf 2010;41(6):759–67.
[6] Di Pasquale G, Motto O, Rocca A, Carter JT, McGrail PT, Acierno D. New high-performance thermoplastic toughened epoxy thermosets. Polymer 1997;38(17):4345–8.
[7] Mallick PK, Broutman LJ. Mechanical and fracture behaviour of glass bead filled epoxy composites. Mater Sci Eng 1975;18(1):63–73.
[8] Moloney AC, Kausch HH, Stieger HR. The fracture of particulate-filled epoxide resins. J Mater Sci 1983;18(1):208–16.
[9] Rosso P, Ye L, Friedrich K, Sprenger S. A toughened epoxy resin by silica nanoparticle reinforcement. J Appl Polym Sci 2006;100(3):1849–55.
[10] Lange F, Radford K. Fracture energy of an epoxy composite system. J Mater Sci 1971;6(9):1197–203.
[11] Sun L, Gibson RF, Gordaninejad F, Suhr J. Energy absorption capability of nanocomposites: a review. Compos Sci Technol 2009;69(14):2392–409.
[12] Moloney AC, Kausch HH, Kaiser T, Beer HR. Parameters determining the strength and toughness of particulate filled epoxide resins. J Mater Sci 1987;22(2):381–93.
[13] Nakamura Y, Yamaguchi M, Okubo M, Matsumoto T. Effects of particle size on mechanical and impact properties of epoxy resin filled with spherical silica. J Appl Polym Sci 1992;45(7):1281–9.
[14] Kitey R, Tippur HV. Role of particle size and filler–matrix adhesion on dynamic fracture of glass-filled epoxy. I. Macromeasurements. Acta Mater 2005;53(4):1153–65.
[15] Fu S-Y, Feng X-Q, Lauke B, Mai Y-W. Effects of particle size, particle/matrix interface adhesion and particle loading on mechanical properties of particulate–polymer composites. Compos Part B: Eng 2008;39(6):933–61.
[16] Jajam KC, Tippur HV. Quasi-static and dynamic fracture behavior of particulate polymer composites: a study of nano-vs. micro-size filler and loading-rate effects. Compos Part B: Eng 2012;43(8):3467–81.
[17] Jajam KC, Tippur HV. Is nanoalways better? static and dynamic fracture study of particulate polymer composites. Dynamic behavior of materials, vol. 12. New York: Springer; 2013. p. 537–44.
[18] Geisler B, Kelley F. Rubbery and rigid particle toughening of epoxy resins. J Appl Polym Sci 2003;54(2):177–89.
[19] Tsai J-L, Huang B-H, Cheng Y-L. Enhancing fracture toughness of glass/epoxy composites by using rubber particles together with silica nanoparticles. J Compos Mater 2009;43(25):3107–23.
[20] Isik I, Yilmazer U, Bayram G. Impact modified epoxy/montmorillonite nanocomposites: synthesis and characterization. Polymer 2003;44(20):6371–7.

[21] Harani H, Fellahi S, Bakar M. Toughening of epoxy resin using hydroxyl-terminated polyesters. J Appl Polym Sci 1999;71(1):29–38.
[22] Jordan J, Jacob KI, Tannenbaum R, Sharaf MA, Jasiuk I. Experimental trends in polymer nanocomposites—a review. Mater Sci Eng A 2005;393(1–2):1–11.
[23] Iijima S. Helical microtubules of graphitic carbon. Nature 1991;354:56–8.
[24] Yu M-F, Lourie O, Dyer MJ, Moloni K, Kelly TF, Ruoff RS. Strength and breaking mechanism of multiwalled carbon nanotubes under tensile load. Science 2000;287(5453):637–40.
[25] Thostenson ET, Ren Z, Chou T-W. Advances in the science and technology of carbon nanotubes and their composites: a review. Compos Sci Technol 2001;61(13):1899–912.
[26] Geng Y, Liu MY, Li J, Shi XM, Kim JK. Effects of surfactant treatment on mechanical and electrical properties of CNT/epoxy nanocomposites. Compos Part A: Appl Sci Manuf 2008;39(12):1876–83.
[27] Kathi J, Rhee K-Y, Lee JH. Effect of chemical functionalization of multi-walled carbon nanotubes with 3-aminopropyltriethoxysilane on mechanical and morphological properties of epoxy nanocomposites. Compos Part A: Appl Sci Manuf 2009;40(6):800–9.
[28] Ma P-C, Mo S-Y, Tang B-Z, Kim J-K. Dispersion, interfacial interaction and re-agglomeration of functionalized carbon nanotubes in epoxy composites. Carbon 2010;48(6):1824–34.
[29] Kim M-G, Moon J-B, Kim C-G. Effect of CNT functionalization on crack resistance of a carbon/epoxy composite at a cryogenic temperature. Compos Part A: Appl Sci Manuf 2012;43(9):1620–7.
[30] Srikanth I, Kumar S, Kumar A, Ghosal P, Subrahmanyam C. Effect of amino functionalized MWCNT on the crosslink density, fracture toughness of epoxy and mechanical properties of carbon–epoxy composites. Compos Part A: Appl Sci Manuf 2012;43(11):2083–6.
[31] Rahman MM, Hosur M, Zainuddin S, Jajam KC, Tippur HV, Jeelani S. Mechanical characterization of epoxy composites modified with reactive polyol diluent and randomly-oriented amino-functionalized MWCNTs. Polym Testing 2012;31(8):1083–93.
[32] Spitalsky Z, Tasis D, Papagelis K, Galiotis C. Carbon nanotube–polymer composites: chemistry, processing, mechanical and electrical properties. Prog Polym Sci 2010;35(3):357–401.
[33] Gojny F, Wichmann M, Köpke U, Fiedler B, Schulte K. Carbon nanotube-reinforced epoxy-composites: enhanced stiffness and fracture toughness at low nanotube content. Compos Sci Technol 2004;64(15):2363–71.
[34] Fidelus J, Wiesel E, Gojny F, Schulte K, Wagner H. Thermo-mechanical properties of randomly oriented carbon/epoxy nanocomposites. Compos Part A: Appl Sci Manuf 2005;36(11):1555–61.
[35] Zhou Y, Pervin F, Lewis L, Jeelani S. Experimental study on the thermal and mechanical properties of multi-walled carbon nanotube-reinforced epoxy. Mater Sci Eng A 2007;452–453:657–64.
[36] Seyhan AT, Tanoğlu M, Schulte K. Tensile mechanical behavior and fracture toughness of MWCNT and DWCNT modified vinyl-ester/polyester hybrid nanocomposites produced by 3-roll milling. Mater Sci Eng A 2009;523(1):85–92.
[37] Hsieh T, Kinloch A, Taylor A, Kinloch I. The effect of carbon nanotubes on the fracture toughness and fatigue performance of a thermosetting epoxy polymer. J Mater Sci 2011;46(23):7525–35.
[38] Tang L-C, Wan Y-J, Peng K, Pei Y-B, Wu L-B, Chen L-M, et al. Fracture toughness and electrical conductivity of epoxy composites filled with carbon nanotubes and spherical particles. Compos Part A: Appl Sci Manuf 2013;45:95–101.
[39] Yang L, Zhang C, Pilla S, Gong S. Polybenzoxazine-core shell rubber-carbon nanotube nanocomposites. Compos Part A: Appl Sci Manuf 2008;39(10):1653–9.
[40] Shukla A, Parameswaran V, Du Y, Évora V. Dynamic crack initiation and propagation in nanocomposite materials. Rev Adv Mater Sci 2006;13(1):47–58.
[41] Evora VMF, Shukla A. Fabrication, characterization, and dynamic behavior of polyester/TiO_2 nanocomposites. Mater Sci Eng A 2003;361(1–2):358–66.
[42] Evora VM, Jain N, Shukla A. Stress intensity factor and crack velocity relationship for polyester/TiO_2 nanocomposites. Exp Mech 2005;45(2):153–9.
[43] Rahman MM, Zainuddin S, Hosur MV, Malone JE, Salam MBA, Kumar A, et al. Improvements in mechanical and thermo-mechanical properties of e-glass/epoxy composites using amino functionalized MWCNTs. Compos Struct 2012;94(8):2397–406.
[44] Marur PR, Tippur HV. Evaluation of mechanical properties of functionally graded materials. ASTM J Test Eval 1998;26(6):539–45.
[45] Jajam KC, Tippur HV. An experimental investigation of dynamic crack growth past a stiff inclusion. Eng Fract Mech 2011;78(6):1289–305.
[46] ASTM, D5045-96. Standard test methods for plane-strain fracture toughness and strain energy release rate of plastic materials: Annual Book of ASTM Standards; 1996. p. 325–33.
[47] Sanford RJ. Principles of fracture mechanics. Upper Saddle River, NJ, USA: Prentice Hall; 2003.
[48] Kirugulige MS, Tippur HV, Denney TS. Measurement of transient deformations using digital image correlation method and high-speed photography: application to dynamic fracture. Appl Opt 2007;46(22):5083–96.
[49] Jajam KC, Tippur HV. Role of inclusion stiffness and interfacial strength on dynamic matrix crack growth: an experimental study. Int J Solids Struct 2012;49(9):1127–46.
[50] Sanford RJ. Application of the least-squares method to photoelastic analysis. Exp Mech 1980;20(6):192–7.
[51] Nishioka T, Atluri S. Path-independent integrals, energy release rates, and general solutions of near-tip fields in mixed-mode dynamic fracture mechanics. Eng Fract Mech 1983;18(1):1–22.
[52] Pearson RA, Yee AF. Influence of particle size and particle size distribution on toughening mechanisms in rubber-modified epoxies. J Mater Sci 1991;26(14):3828–44.